A simplified method for the detection of convection using high resolution imagery from GOES-16

Yoonjin Lee[1], Christian D. Kummerow[1,2], Milija Zupanski[2]

[1]Department of Atmospheric Science, Colorado state university, Fort Collins, CO 80521, USA
[2]Cooperative Institute for Research in the Atmosphere, Colorado state university, Fort Collins, CO 80521, USA

Correspondence to: Yoonjin Lee (ylee@atmos.colostate.edu)

Abstract. The ability to detect convective regions and adding heating in these regions is the most important skill in forecasting severe weather systems. Since radars are most directly related to precipitation and are available in high temporal resolution, their data are often used for both detecting convection and estimating latent heating. However, radar data are limited to land areas, largely in developed nations, and early convection is not detectable from radars until drops become large enough to produce significant echoes. Visible and Infrared sensors on a geostationary satellite can provide data that are more sensitive to small droplets, but they also have shortcomings: their information is almost exclusively from the cloud top. Relatively new geostationary satellites, Geostationary Operational Environmental Satellites-16 and -17 (GOES-16 and GOES-17), along with Himawari-8, can make up for some of this lack of vertical information through the use of very high spatial and temporal resolutions. This study develops two algorithms to detect convection at vertically growing clouds and mature convective clouds using 1-minute GOES-16 Advanced Baseline Imager (ABI) data. Two case studies are used to explain the two methods, followed by results applied to one month of data over the contiguous United States. Vertically growing clouds in early stages are detected using decreases in brightness temperatures over ten minutes. For mature convective clouds which no longer show much decreases in brightness temperature, the lumpy texture from rapid development can be observed using 1-minute high spatial resolution reflectance data. Detection skill of the two methods are validated against MRMS, a ground-based radar product. With the contingency table, results applying both methods to one month data show a relatively high accuracy of 85.6% but missed 54.7% of convective clouds detected by the radar product. These convective clouds are largely under optically thick cloud shields, and thus missed from analysing lumpy textures.

1 Introduction

While weather forecast models have improved tremendously throughout the decades (Bauer et al., 2015), local scale phenomena such as convection remain challenging (Yano et al., 2018). Precipitation is especially hard to predict as numerical models struggle with initiating convection in the right location and intensity. To address this issue in short term predictions, many models now assimilate all-sky radiances and precipitation-related products where available (Benjamin et al., 2016; Bonavita et al., 2017; Geer et al., 2017; Gustafsson et al., 2017; Jones et al., 2016; Migliorini et al., 2018; Scheck et al., 2020). In some forecast models such as the High Resolution Rapid Refresh (HRRR) model in the United States, latent heating is added, along with precipitation affected radiances, to adjust model dynamics to correspond to the observed convection (Benjamin et al., 2016). Latent heating is only added in convective regions because local scale phenomena tend to develop first by convective clouds before detraining stratiform precipitation. In order to correctly detect convective regions and add heating as frequent as possible, ground-based radars have been used during the short-term forecast. This study explores whether high temporal resolution data from recent operational geostationary satellite, Geostationary Operational Environmental Satellites (GOES) – R Series, can provide similar information to initialize forecast models.

Convection is classically defined from in-cloud vertical air motions (Steiner et al., 1995). However, since vertical velocity is rarely measured directly, the radar community initially adopted radar reflectivity thresholds to define convection and distinguish

40   it from stratiform precipitation (Churchill and Houze, 1984; Steiner et al., 1995). One problem with using reflectivity threshold is its sensitivity to the selected threshold for convection. If the threshold is set high, convective regions where precipitation has just begun are not captured, while a threshold that is set too low will misclassify some stratiform regions as convective. To address this issue, Churchill and Houze (1984) separated precipitation types by using the horizontal structure of precipitation fields (Steiner et al., 1995). They classified a grid point as convective if the grid point had rain rates twice as high as the average taken

45   over surrounding grid points or had reflectivity over 40dBZ ($\sim$ 20 mm h^{-1}). Steiner et al. (1995) refined this method with three criteria: intensity, peakedness, and surrounding area. They used the same threshold of 40dBZ for intensity, but used variable thresholds for reflectivity differences between convective cores and surrounding areas depending on the mean background reflectivity. Nonetheless, stratiform regions sometimes can have reflectivity values greater than 40dBZ. Zhang et al. (2008) used two reflectivity criteria for convective precipitation-namely that the reflectivity be greater than 50dBZ at any height and greater

50   than 30dBZ at -10°C or higher. Zhang and Qi (2010) used a vertically integrated liquid water field and had a single threshold of 6.5kg m^{-2}. Qi et al. (2013) developed a new algorithm that combined two previous methods from Zhang et al. (2008) and Zhang and Qi (2010). By combining these two methods and modifying the thresholds, they were able to decrease misclassification of stratiform regions with strong bright band features, but could still miss some convective regions in their initial stage due to a high reflectivity threshold. The HRRR model uses a much lower reflectivity threshold of 28dBZ to detect convective regions and

55   assigns a heating increment (Weygandt et al., 2016). While this is significantly lower than the thresholds discussed above, its primary purpose is to initiate convection where there is significant echo present, while relying on the model physics to assign the proper precipitation type.

While radars have been the preferred method for detecting convection, they are not the only instruments available. Visible (VIS)

60   and infrared (IR) radiances also contain some information, although largely limited to cloud top properties. Convection detection algorithms using VIS and IR sensors exist for both convective initiation (CI) and mature stages. At the initial stages of convection, cloud tops grow vertically, and decrease in T_b is observed accordingly. Many algorithms use decreased cloud top temperature from the growth (related to the in-cloud vertical velocity) to detect convective regions from various geostationary satellites over the globe such as GOES (Sieglaff et al., 2011; Mecikalski and Bedka, 2006), Himawari-8 (Lee et al., 2017), and

65   Meteosat (Autonès and Moisselin, 2010). Temporal trends of T_b are evaluated on several channels around water vapor absorption band or longwave infrared window band and combinations of these channels. Interest fields for CI include temporal trend of T_b at 10.7µm (or 11.2µm) to infer cloud top cooling rates, (3.9µm – 10.7µm) to infer changes in cloud top microphysics, and (6.5µm – 10.7µm) to infer cloud height changes relative to the tropopause (Mecikalski and Bedka, 2006). Main differences between the algorithms are tracking method of a cloud and time period used to calculate T_b change of the cloud. Clouds are usually tracked

70   with atmospheric motion vectors or a simple overlap method, and temporal trends of T_b are calculated over 15 minutes.

Convective clouds in their mature stage cannot be detected by the abovementioned algorithms as their cloud tops do not grow much in the vertical, and T_b decrease is not a main feature that is applicable to such clouds. Overshooting Top (OT) is one of the clear indications of mature convective clouds, and many existing algorithms used OT feature in such clouds. There are two

75   common approaches to detect OTs: the brightness temperature difference method and the infrared window-texture method (Ai et al., 2017). The brightness temperature difference method uses a difference in T_b between the water vapor (WV) channel and IR

window channel ($T_{b,wv} - T_{b,IR}$). Positive values of $T_{b,wv} - T_{b,IR}$ due to the forcing of warm WV from below into the lower stratosphere are used as an indicator of OTs (Setvak et al., 2007). However, since the threshold for the difference between two channels can depend on several factors, Bedka et al. (2010) suggested another method to detect OTs which is called the Infrared window-texture method. This method takes advantage of a feature of OT in that it is an isolated region with cold T_b surrounded by relatively warm anvil region (Bedka et al., 2010). This method, unfortunately, cannot avoid having to choose T_b thresholds that vary according to seasons or regions (Dworak et al., 2012). Bedka et al. 2016 tried to minimize the use of fixed detection criteria. They developed two OT detection algorithms based on IR and VIS channels, and an OT probability was produced through a pattern-recognition scheme. The pattern that the scheme looks for is protrusion through the anvil caused by strong updrafts. Another pattern that is obvious in mature convective clouds with or without OT is "lumpy surface" from constant bubbling (Mecikalski and Bedka, 2006). Cloud top texture in VIS and IR channels has been explored using Spinning Enhanced Visible and Infrared Imager (SEVIRI) on Meteosat satellite in Zinner et al. 2008 and Zinner et al. 2013, respectively. In addition to evaluating spatial texture, Müller et al. (2019) explores spatio-temporal gradients of water vapor channels in SEVIRI to estimate updraft strength.

The use of VIS and IR sensors in detecting convection can benefit significantly with the launch of National Oceanic and Atmospheric Administration's (NOAA's) GOES-R Series which have high resolution, rapidly updating (i.e. 1 minute) imagery. This study makes use of this new data, namely the 1 minute data available from GOES-16 and GOES-17 in "mesoscale sectors" to update methods for detecting convection in different stages. One is developed for CI using T_b from an IR channel in GOES-R. As in previous papers measuring clout top cooling rate, temporal trends of the data were used but, since GOES-R has high temporal resolution, ten consecutive data with 1-minute interval were used. This procedure eliminates errors from cloud movements that needed to be dealt with in some previous studies, and cooling rate is calculated applying linear regression on 1-minute data over 10 minutes, rather than using T_b difference between 15 minutes. Another one is developed for mature convection using both reflectances from a VIS channel and T_b. For this algorithm, lumpy and rapidly changing surface and high cloud top height from mature convective clouds were used to detect clouds both with and without OTs. Lumpiness is calculated using Sobel operator which is an edge detection filter in image processing, and the lumpiness is explored at each minute throughout 10 minutes to look for regions with continuous bubbling. These two methods were then combined to provide detection of convection in all stages. The above methods are not intended to replace ground-based radars where these are available. Instead, the focus here is complementing ground-based networks, either off-shore or other regions lacking coverage.

The datasets that were used to detect convection and validate the results are described in Sect. 2, while the methods used to identify initial and established convection are explained in Sect. 3. Sect. 4 highlights the results of each method. Two case studies were examined followed by a one-month statistical study to quantify the operational accuracy of the methods.

2 Data

2.1 The Geostationary Operational Environmental Satellite R series (GOES-R)

Earth-pointing instruments of GOES-R consist of the Advanced Baseline Imager (ABI) with 16 channels, and the Geostationary Lightning Mapper (GOES-R Series Data Book, 2019). GOES-16 is the first of the two GOES-R series satellites to provide data for severe weather forecast over the United States and surrounding oceans (Smith et al., 2017). Both T_b and reflectance data from the ABI were used to detect convective regions. Mesoscale data with one minute temporal resolution were used to fully exploit its high temporal resolution of the new instrument.

Reflectance at 0.64μm (Channel 2) and T_b at 6.2μm (Channel 8), 7.3μm (Channel 10), and 11.2μm (Channel 14) were used in the study. Channel 2 is a "red" band with the finest spatial resolution of 0.5km. This fine spatial resolution is useful to resolve lumpy, or bubbling surfaces of clouds in their mature stage. Channel 2 reflectance data were normalized by solar zenith angle so that a single threshold can be used throughout the method regardless of locations of the sun. Channel 14 is an IR longwave window band, which is a good indicator of the cloud top temperature for cumulonimbus clouds (Müller et al., 2018). High reflectance and texture of the cloud top seen in channel 2 and cloud top height inferred from channel 14 are combined to determine locations of mature convective clouds.

Channel 8 and 10 are ABI water vapor channels with 2km spatial resolution. Because Channel 8 sees WV at somewhat higher altitudes than Channel 10, they can observe WV associated with updrafts as they progress upwards, and were therefore used to detect early convection.

2.2 NEXRAD and MRMS

Multi-Radar/Multi-Sensor (MRMS) data developed at NOAA's National Severe Storms Laboratory were used for validation purposes. MRMS integrates the radar mosaic from the Next Generation Weather Radar (NEXRAD) with atmospheric environmental data, satellite data, lightning, and rain gauge observations to produce three dimensional fields of precipitation (Zhang et al., 2016). These quantitative precipitation estimation (QPE) products have a spatial resolution of 1km and temporal resolution of 2 minutes.

A "PrecipFlag" variable contained in the standard MRMS product classifies precipitating pixels into seven categories: 1) warm stratiform rain, 2) cool stratiform rain, 3) convective rain, 4) tropical–stratiform rain mix, 5) tropical–convective rain mix, 6) hail, and 7) snow. Details of the classification can be found in Zhang et al. (2016). A reduced set of these classes were used to validate the convective classification from GOES ABI data. In this study, warm stratiform rain, cool stratiform rain, and tropical-stratiform rain mix are all assigned a stratiform rain type while grid points with convective rain, tropical-convective rain mix, and hail are assigned a convective rain type. It is a rather sophisticated classification of precipitation type as it not only uses reflectivity at various heights, but also takes into account vertically integrated liquid to distinguish convective core from stratiform clouds (Qi et al., 2013). Along with the classification product, MRMS provides a variable called "Radar QPE quality index (RQI)". This product is associated with quality of the radar data, which is a combination of errors coming from beam blockages and the beam spreading/ascending with range (Zhang et al., 2016). This flag is used to mask out regions with low radar data quality. Only data with RQI greater than 0.5 are used in this study.

3 Methodology

This study examines methods to detect convective clouds at each life stage. Convective clouds can be divided into actively growing clouds and mature clouds. Actively growing clouds are usually clouds at the initial stage that grow nearly vertically while mature clouds are capped, but continue to bubble due to the release of latent heat. They often move horizontally after they reach the tropopause. The proposed method to detect actively growing cloud is similar to the GOES-R CI algorithm in the sense that the method uses temporal trends of T_b. The high temporal resolution data simplifies the method because the use of derived wind motion in tracking clouds is no longer necessary. One minute is short enough that cloud motion, at most, is to the adjacent grid points, and clouds can be easily tracked by focusing on overlapped scenes.

155 The method to detect mature convective clouds is similar to previous studies by Bedka et al. 2016 and Bedka et al. 2019 in terms of using the texture of the cloud top surfaces to infer strong updrafts. Cloud top surfaces of mature convective clouds are much bumpier than any other clouds, and their bumpiness is most evident in VIS images with the finest resolution. The following method uses horizontal gradients of reflectance to represent the bumpiness of cloud tops, and the magnitude of the gradients are used to distinguish convective cores from their anvil clouds. Cloud top temperatures from channel 14 are used to eliminate low

160 cumulus clouds that might appear bubbling.

3.1 Detection of actively growing clouds with brightness temperature data

In the early stage of convection, updrafts of water vapor eventually lead to condensation, the release of latent heat, and convective processes. Operational weather radars cannot observe small cloud water, but water vapor absorption bands in GOES-ABI, are more sensitive to these small droplets. During the early convective stages, T_bs that are sensitive to water vapor will decrease due

165 to condensed cloud water droplets aloft generated by a strong updraft. Two ABI channels around the water vapor absorption bands, channel 8 (6.2μm) and channel 10 (7.3μm), were selected to cover water vapor updrafts at different height levels. These channels were used to find small regions consistent with developing clouds. If a cloud develops continuously for ten minutes and shows a large decrease in T_b over ten minutes in either channel, the cloud is determined to be convective.

170 To compute the T_b decrease in clouds, a window has to be defined as it is usually difficult to precisely define the boundary of clouds, especially at the early stages of convection. Since most of the early convective clouds are smaller than 10km in diameter, the window was defined as a 10km×10km box which is essentially a 5×5 matrix of satellite pixels consisting of 25 T_bs with 2km resolution. Considering the fact that a convective core usually has the lowest T_b within its neighborhood, the T_b matrix was formed around a pixel only if that pixel had the lowest T_b in the 5×5 matrix. However, this criterion alone could not distinguish

175 convective cores from stratiform clouds and cloud edges which can also exhibit a local minimum. In addition to the lowest T_b, the shape of convective clouds is therefore also considered. As shown in the Fig. 1a, convective clouds not only have the lowest T_b in their cores in all directions, but also have increasing T_bs away from the core, making their T_b distributions look like an inverted two-dimensional (2D) Gaussian distribution. To select T_b matrices that have this inverted Gaussian shape, an inverted 5×5 Gaussian matrix that has mean and standard deviation of the T_b matrix was created and compared with the T_b matrices. To focus

180 the comparisons on the shape of the T_b distribution (Fig. 1b), the maximum T_b found in the 5×5 matrix was subtracted from all values, and T_b values were divided by the difference between maximum and minimum T_b to normalize the T_b matrix itself. If the T_b matrix has a shape of a developing cloud (i.e. 2D inverse Gaussian), the absolute value of the difference between the T_b matrix and the inverse Gaussian matrix will be small. A threshold of 10 for this absolute value of the difference between T_b shape and inverse Gaussian shape (sum of residuals between normalized T_b and inverse Gaussian) was empirically determined to exclude

185 non-convective scenes. T_b matrices with values greater than 10 are removed from the scene. This is done for all ten consecutive T_b images that are one minute apart. Continuous overlaps of T_b matrices for ten minutes imply that the cloud maintained a convective shape for ten minutes, and therefore, changes in T_b are calculated to assess if the cloud in the T_b matrices was growing.

190 The minimum T_bs of the T_b matrices at each time step were linearly regressed against time to measure a decreasing trend. Since one-minute data can be noisy, the decreasing trend was considered instead of an actual difference in T_b during 10minutes. If the fitted line had a slope smaller than -1K/min for channel 10 or -0.5K/min for channel 8, the grid point with the lowest T_b at each

time step for ten minutes as well as the neighboring 8 grid points in the window were classified as convective. The threshold of -1K/min and -0.5K/min were determined empirically, and choosing these thresholds are elaborated in section 4.3. Some convective clouds in the early stage show smaller decreasing trend, but using a smaller value for the threshold can introduce clouds that do not grow into deep convective clouds in the end. Clouds that develop into deep convective clouds are eventually captured by these thresholds in later times as they show rapid intensification sooner or later. Actively growing clouds are usually detected by channel 10 first and then by channel 8. This makes sense because channel 10 sees water vapor in lower parts of the atmosphere while channel 8 sees upper level water vapor. Using two channels help find the same clouds in different levels.

3.2 Detection of mature convective clouds with reflectance data

Mature convective clouds consist of convective cores and stratiform or cirrus regions where clouds have detrained from the core. The lack of discrete boundaries between different types of clouds make it difficult to separate convective grid points from surrounding stratiform regions. Overshooting tops and enhanced-V pattern are well-known features in mature convective clouds, but these do not appear until their strongest stage and not in all convective clouds. Using such features associated with the deepest convective cores will create a detection gap between early and mature stages of convection. The method described here tries to minimize the gap, while still accurately detecting convective clouds.

A distinct feature that appears in convective clouds, even in their early stages, is a bubbling cloud top. The lumpiness of cloud tops can be numerically represented by calculating horizontal gradients in the reflectance field with the Sobel-Feldman (Sobel) operator which is commonly used in edge detection. The horizontal gradient is calculated at each pixel. The Sobel operator convolves the target pixel and its surrounding eight grid points with two kernels given in Eq. (1) to produce gradients in the horizontal and vertical direction.

$$G_x = \begin{bmatrix} +1 & 0 & -1 \\ +2 & 0 & -2 \\ +1 & 0 & -1 \end{bmatrix} \quad G_y = \begin{bmatrix} +1 & +2 & +1 \\ 0 & 0 & 0 \\ -1 & -2 & -1 \end{bmatrix} \quad (1)$$

By using Eq. (2), gradients in each direction are combined to provide the absolute magnitude of the gradient at each point.

$$\text{Magnitude of gradient} = \sqrt{G_x^2 + G_y^2} \quad (2)$$

Flat surfaces will have low gradients while cloud edges or lumpy surfaces will have high gradients. This lumpy feature is most evident in a VIS channel with the finest spatial resolution of 0.5km. IR fields are not very useful as the brightness temperature variations in these lumpy surfaces tend to be quite small relative to the IR's 2km resolution, and only cloud edges stand out.

Before evaluating the texturs, only the grid points that are potentially parts of deep convection are selected using simple threshold values of VIS (ABI channel 2; 0.65μm) and IR (ABI channel 14; 11.2μm) channels. Channel 2 reflectance is highly correlated with the cloud optical depth (Minnis and Heck, 2012) while Channel 14 brightness temperature is related to cloud top temperature (Müller et al., 2018). These channels are used in GOES-R baseline product retrieval of cloud optical depth and cloud top properties, respectively. Any grid points with reflectance less than 0.8 or T_b greater than 250K during ten time steps (10 minutes) are removed since they generally represent thin or low clouds such as cirrus or growing clouds that can be identified by the CI method described earlier. These thresholds are chosen rather generously to include some convective clouds that have not

grown into deep convection yet, while still avoiding the misclassification of low cumulus clouds and thin anvil clouds as convective. The threshold of 250K is much warmer than typical values used in detecting deep convective features such as overshooting tops (Bedka et al., 2010) or enhanced-V (Brunner et al., 2007). Warmer threshold is intentionally chosen so that the method considers warmer convective clouds without those features in the next step when evaluating lumpiness of the cloud top. The choice of these thresholds is discussed in more detail in section 4.3.

Once cold, highly reflective scenes are identified, the horizontal gradients of reflectance are calculated using the Sobel operator. The average of the horizontal gradients over the ten 1-minute time steps is calculated for each grid point, and grid points are removed if the average was less than 0.4 or greater than 0.9. Values below 0.4 or above 0.9 generally implies either stratiform region with a flat surface or cloud edges with very high gradients. The remaining grid points were then interpolated into 1km maps to be consistent with the spatial resolution of MRMS dataset. Neighboring grid points were grouped to form clusters, and only the clusters with more than 5 grid points were assigned as a mature convective cloud to remove noise.

4 Results and Discussion

We begin the result section with two case studies that illustrate the technique as well as some of its limitations.

4.1 June 28th, 2017

Supercell thunderstorms developed in Iowa and produced several tornado touchdowns. In Fig. 2a, deep convection had already developed over central Iowa at 19:30UTC, and two convective cells in the red box started to develop in southeast Iowa, although they do not stand out from surrounding low clouds in the VIS image. These two convective clouds became parts of major storm system that formed around 21:30UTC, producing the tornadoes (Fig. 2b) in the area. The two cells appeared in the Omaha (KOAX), Des Moines (KDMX), and La Crosse (KARX) NEXRAD radars at 19:30UTC (Fig. 2c), but reflectivity was very weak ($\leq$ 30dBZ). In addition, the MRMS PrecipFlag product is shown in Fig. 2d. Convection is colored in pink and stratiform in green. Although deep convections over central and northeast part of Iowa were assigned as convective in MRMS at 19:30UTC, the two growing clouds in the red box in Fig. 2a were not assigned convective flag until 19:48UTC.

Figure 3a shows brightness temperatures for ABI channel 10 at 19:27UTC. The two growing convective cells in the white circle are shown in barely visible yellow surrounded by high T_bs. The one on the left was detected using 10-minute data from 19:25UTC, but since both clouds were detected starting at 19:27UTC, a scene from 19:27UTC was used to demonstrate the method. Figure 3c and 3d show T_b matrices that exhibited the correct shape for developing cells (Gaussian shape) at 19:27UTC and 19:36UTC. However, not all of the matrices in these figures showed the evolution of the developing cells (decreasing minimum T_b over 10K) between the two time steps. The only two matrices in this scene that satisfied both criteria of maintaining the shape of developing cells and growing vertically over ten time steps were the two in blue circles. These two matrices contain early convective clouds that grow into deep convection shown in Fig. 2b, and they are correctly captured by this method.

Results for the detection of mature convective clouds are shown in a step by step fashion in Fig. 4. Figure 4a is the same as in Fig. 2a, but is mapped using a different color table for better comparisons between steps. Figure 4b shows the pixels retained after eliminating all the grid points that did not meet the reflectance and T_b thresholds (minimum reflectance over ten time steps greater than 0.8 and maximum T_b over ten time steps less than 250K). Figure 4c shows the horizontal gradient values after applying the Sobel operator. The colorbar is set to be within the range of 0.4 and 0.9 to display potential convective regions that

passed these thresholds in colors. White regions are either regions that have average gradients greater than 0.9 such as cloud edges or thin cirrus clouds, or regions that have average gradients less than 0.4 such as clear sky or stratiform regions. Eventually, only the regions that meet both the criteria in Fig. 4b and 4c are assigned to convection, and shown as white shade in Fig. 4d. Using reflectance threshold sometimes limits detecting shaded convective regions that exhibits lower reflectance than the threshold of 0.8, and white regions surrounded by colored regions in Fig. 4b are such regions. However, these regions are relatively small, and once they are upsampled into 2km map with nearest neighbour interpolation, some of these regions are included in the detection as shown in Fig. 4d.

For a better comparison between detection from GOES and MRMS, convective regions detected by GOES (Fig. 4d) are parallax corrected with a constant cloud top height of 10km and plotted on top of the MRMS map (Fig. 2d), and it is shown in Fig. 5. Most of convective regions align well with high reflectivity regions in Fig. 2c and convective regions in Fig. 2d. However, a straight line around 44N at the right edge of Fig. 4d is definitely not a convective region, and it is due to unrealistically high reflectance in the raw satellite dataset. These kinds of artifacts were removed later in section 4.3 when the method was applied to a full month of data. However, multiple lines are difficult to remove at this stage in the processing and will result in false alarm. As quality control procedures on ABI are improved, this may no longer be a source of significant errors.

4.2 June 18th, 2018

Another case was examined to evaluate the methods under different conditions. Severe storms developed over the Great Plains in June 18th, 2018, producing hail on the ground. At 22:30UTC, sporadic storms across Kansas and Oklahoma were observed by GOES-16. This scene contains both growing and mature convective clouds, and MRMS PrecipFlag for the scene is shown in Fig. 6a and 6b. Green color represents stratiform and pink color represents convective clouds. Figure 6c and 6d are brightness temperature maps of the same scene at 22:30UTC and 22:40UTC, respectively. Growing clouds shown in purple, blue, yellow, and green boxes are detected by the T_b method, but all starting from different time. Convection in the purple box is detected using ten consecutive T_b data starting at 22:19UTC. Considering the last data used at 22:28UTC, it was detected six minute earlier than MRMS detection which was at 22:34UTC. The growing cloud in the blue box was detected 7 minute after MRMS detection at 22:38UTC. This cloud did not grow rapidly enough and did not meet the T_b threshold for channel 10 at the onset of convection. However, it was detected by channel 8 as it grew higher altitudes. This shows a need to use both channels in the detection. Similarly, a cloud in the green box was detected by channel 8 starting at 22:27UTC. Although it precipitated, this cloud did not grow into a severe storm. The growing cloud in the yellow box was detected by GOES using data from 22:29UTC and detected by MRMS at 22:38UTC. These results show that even though the thresholds for the T_b method can miss some convective clouds that grow slowly in the beginning, the thresholds were adequate for detecting rapidly growing convective storms which are of more interest during the forecast.

Black regions superimposed on the brightness temperature map in Fig. 6c represent convective regions identified by the mature convection method. There are slight misalignments of detected convective clouds between MRMS PrecipFlag products and GOES results possibly due to sheared vertical structures of the storms, but overall, they seem to match well.

4.3 Statistical results with one-month data

Statistical verification of the two methods is conducted using one month of data during June of 2017. Results are validated against MRMS data as ground-based radar is used to detect convective regions during the short-term forecast, and precipitation is

a rather direct indicator of convection in all stages. Table 1 is a contingency table applying both methods to one month data. C represents convection detected by either GOES or MRMS, and NC represents non-convective regions. GOES-C/MRMS-C is "hits" that both MRMS and GOES methods detected as convective within 5km. In case of the T_b method, on the other hand, hits are defined if MRMS assigned convective within 30 minutes due to earlier detection by this method. GOES-NC/MRMS-C is "misses" that GOES missed detecting convection while MRMS assigned as convective. GOES-C/MRMS-NC is "false alarm" that GOES detected as convective, but MRMS did not. Lastly, GOES-NC/MRMS-NC is "correct negative case" that both MRMS and GOES did not detected as convective. From the contingency table, verification metrics of probability of detection (POD) and false alarm rate (FAR) can be calculated as below.

$$POD = \frac{hits}{hits + misses} \qquad FAR = \frac{false\ alarm}{hits + false\ alarm}$$

POD and FAR are useful tools in evaluating detection skill of a binary problem. POD and FAR calculated from Table 1 are 45.3% and 14.4%. Since POD and FAR can vary depending on the thresholds used in each method, choosing different thresholds is examined further.

Most of the detection is from the reflectance method as mature convective clouds account for much larger area. The reflectance method alone has FAR of 14.2% and POD of 43.7%. Low FAR is achieved after comparing results using different combinations of the three thresholds (reflectance at channel 2 and T_b at channel 14 to remove shallow and low clouds, and horizontal gradients of reflectance at channel 2 to remove cloud edges as well as clouds with flat cloud top surfaces). Two thresholds for cloud top texture, which is essentially horizontal gradients of reflectance, are evaluated first. The upper threshold does not change results much (not shown), and cloud edges are effectively removed by the threshold of 0.9. The lower bound of the texture thresholds are varied, keeping the upper threshold and the T_b and reflectance thresholds constant. Resulting FAR and POD are shown in Fig. 7. Using 0.5 (yellow) misses significant amounts of convective regions while using lower values (blue and red) substantially misclassifies stratiform regions with flat cloud tops as convective, although their PODs are much higher. From this, a value of 0.4 (green diamond in Fig. 7) was chosen as a reasonable compromise between POD and FAR.

POD and FAR using different combinations of T_b and reflectance thresholds are plotted in Fig. 8, and this time texture thresholds are kept constant with 0.4 and 0.9. The T_b threshold is varied from 230K to 250K, and the reflectance threshold is varied from 0.7 to 0.9. There is a trade-off between detecting more mature convective clouds in the earlier stage and incorrectly assigning cumulus clouds as convective clouds. Having lower value for the T_b threshold or higher value for the reflectance threshold leads to small FAR, but also leads to small POD. To make this method effective and reduce FAR as much as possible for its potential use in the short-term forecast, 250K for the T_b and 0.8 for the reflectance threshold (black diamond in Fig. 8a) are chosen. 240K and 0.7 (orange) also showed similar results, but 250K and 0.8 were chosen due to lower FAR. Figure 8b shows results including MRMS data 10 minutes after the detection period. Even though this method is mainly for convective clouds that are mature enough to produce precipitation and observed by radar at the time of detection, Fig. 8b still shows its ability to detect convection earlier than MRMS. Most of the results showed improvements in both FAR and POD (lower FAR and higher POD) when later data are included.

Despite its FAR being relatively small, the method misses significant amounts of convective areas observed by MRMS. Therefore, regions that were missed are evaluated further to investigate which threshold contributed most to missing those

345 regions. Figure 9 shows histograms of T_b, reflectance, and texture in the convective regions that were missed by the above method. It is clear from the figure that the largest number of misses were due to low texture values (87.6% of all missed regions has lower gradients than 0.4). There are many reasons why convective regions appear to have flat cloud top surfaces. Anvil or thick cirrus clouds above convective regions can smooth out or cover bubbling cloud tops, and there is simply no way to avoid this problem. Another reason may be the nature of the classification method. Since classification by MRMS is determined by rain

350 rate, even if convective clouds are in a decaying mode and do not bubble anymore, clouds can still continue to precipitate considerable amounts, which would lead to convective category in the MRMS product. It is also possible that it is due to a misclassification of trailing stratiform regions using radars. It is indeed an ongoing research in the radar community since better convective/stratiform classification scheme improves QPE retrieval (Qi et al., 2013; Veljko et al., 2019).

355 Contrarily, the T_b method for detecting early convection only requires one threshold of T_b decrease. However, since water vapor channels have different sensitivity to water vapor, different values for the threshold are required for each channel (channel 8 and 10). Since growth rate can vary depending on the surrounding environment and different evolution stages, it is important to find an appropriate threshold that best represents growth rate for clouds in their early stages. In order to investigate proper values, the 5×5 T_b windows that maintained the developing shape and had a decreasing trend of T_b during ten minutes are collected over the

360 one month period. A total of 27971 and 73204 (for channel 8 and 10, respectively) 5×5 windows were collected, and precipitation types from MRMS were assigned for each window. Future MRMS convective flags up to 30 minutes were included in the analysis because some time delays were observed in MRMS product when assigning convective flags, especially for early convection. When comparing GOES products to future MRMS products, future locations of GOES products were calculated assuming convection moves at the same speed that clouds moved during the initial ten minutes. Tables 2 and 3 show results

365 applying different thresholds ranging from -0.1K/min to -2.0K/min. Numbers in the table represent the number of 5×5 windows that MRMS precipitation flags were assigned to either non-convective or convective at the corresponding 10-minute time window, as well as pixels that were flagged as convective by MRMS in the next 20 minutes to account for the fact that GOES can detect convection before the radar sees precipitation. For channel 8, using a threshold less than -1.4K/min has 100% accuracy of detecting convection as in MRMS, but in return, it misses much of the convection and loses an ability to detect convection earlier

370 than radar because not all convective clouds have such a strong updraft. Thresholds are chosen so that it achieves at least 85% accuracy and detects reasonable amounts of convections. Therefore, -0.5K/min and -1.0K/min are chosen for channel 8 and 10, respectively. Growth rate observed at channel 8 is smaller than channel 10 due to higher absorption at channel 8. Channel 8 senses moisture at higher altitude and thus, when water vapor starts to condensate at lower levels, it is less affected, and its T_b does not decrease as much as in channel 10. As clouds grow thicker, signals in water vapor absorption bands are dominated by

375 the clouds, less from water vapor, and their T_bs becomes similar. Therefore, it makes sense again that the growth rate at channel 10 has to be bigger to catch up lower T_b in channel 8. It is interesting to note that some clouds did not produce precipitation even with rapid growth over -2.0K/min (for channel 10). This would be due to mixing between convective cells and their dry environment or highly non-linear nature of chances of precipitation.

380 As shown from these results, there are no perfect thresholds that can separate convective and stratiform clouds. Nevertheless, threshold values were chosen based on our purpose, which are to avoid high FAR as much as possible and have decent POD comparable to radar products. Avoiding FAR is a higher priority than reaching higher POD as giving false information is most detrimental during data assimilation. Although large amounts of convective area assigned by radar product are missed due to intrinsic problem of using VIS and IR bands and mainly using cloud top texture to distinguish from stratiform clouds, low FAR

385 of 14.4% is achieved, and 96.4% of false alarm pixels are at least raining. Since the main objective of data assimilation is to have good prediction of precipitation, applying these methods during data assimilation can still be beneficial in case the forecast model did not produce precipitation.

5 Conclusion and summary

390 This study explores two methods to detect convective clouds using GOES-R ABI data with one minute interval. Using such high temporal resolution data facilitates cloud tracking and helps the accuracy of the detection method when calculating decreases in T_b of the same cloud. Convective clouds in the early stage were detected using T_bs of ABI channels 8 and 10. These channels were used to find cloud scenes with the developing shape of convective clouds. They were then used again to calculate the T_b decrease for those which maintained the developing shape for ten minutes. A cloud scene that had a consistent developing shape 395 and a large decrease in T_b over ten minutes was classified as convective by this method. Mature convective clouds were detected by masking out regions with high T_b in ABI channel 14 and low reflectance in ABI channel 2 and finding regions with high horizontal gradients of reflectance over the course of ten minutes. Results from this reflectance method were mostly consistent with the radar-derived products, although this method is limited to daytime use only. Nevertheless, it detects a wide range of convective area, not just regions with overshooting tops.

400

These methods work well for well-structured convective clouds, but there are limitations to this method as with most algorithms using IR and VIS sensors have. Cirrus cloud shields are the biggest problem as they block T_b decreases underneath and smooth out lumpy reflectance surfaces. However, these methods can still be extremely useful for defining convection for assimilation into models where radar data is not available. Because regions identified as convective are most likely convective (~85% 405 accuracy), this can easily be assimilated while setting cloudy regions to "missing" since the accuracy of detecting convection under large cirrus shields is poor. Furthermore, results using Sobel operator, which is commonly used in image processing, implies that applying machine learning can be beneficial if the model can be set up to learn lumpy texture of convective clouds during training.

Author contributions

410 All three authors designed the experiments. YL processed and analysed the data. CK and MZ gave feedbacks with their insights at every step of the data analysis. The manuscript was written jointly by YL, CK, and MZ.

Competing interests

The authors declare that they have no conflicts of interests.

Data availability

415 NEXRAD reflectivity data were obtained by NOAA's National Centers for Environmental Information: doi:10.7289/V5W9574V. Past MRMS datasets are available at http://mtarchive.geol.iastate.edu/. GOES-R data were made available by Cooperative Institute for Research in the Atmosphere (CIRA).

Acknowledgement

This research is supported by CIRA's Graduate Student Support Program, as well as the WMO sponsored ICEPOP-18 project
420   through the Korean Meteorological Administration.

References

Ai, Y., Li, J., Shi, W., Schmit, T. J., Cao, C., and Li, W.: Deep convective cloud characterizations from both broadband imager and hyperspectral infrared sounder measurements, J. Geophys. Res., 112, 1700-1712, doi: 10.1002/2016JD025408, 2017.

Bauer, P., Thorpe, A., and Brunet, G.: The quiet revolution of numerical weather prediction, Nature, 525, 47-55, doi:
425   10.1038/nature14956, 2015.

Autonès, F. and Moisselin, J.-M.:   Algorithm Theoretical Basis Document for "Rapid Development Thunderstorms. Scientific documentation of SAF/NWC PGE 11 (RDT) v2011, code SAF/NWC/CDOP/MFT/SCI/ATBD/11, available on http://www.nwcsaf.org/

Bedka, K., Brunner, J., Dworak, R., Feltz, W., Otkin, J., and Greenwald, T.: Objective satellite-based detection of overshooting
430   tops using infrared window channel brightness temperature gradients, J. Appl. Meteorol., 49, 181-202, doi: 10.1175/2009JAMC2286.1, 2010.

Bedka, K. and Khlopenkov, K.: A probabilistic multispectral pattern recognition method for detection of overshooting cloud tops using passive satellite imager observations, J. Appl. Meteorol. Climatol., 55, 1983-2005, doi: 10.1175/JAMC-D-15-0249.1, 2016.

Bedka, K., Yost, C., Nguyen, L., Strapp, J.W., Ratvasky, T., Khlopenkov, K., Scarlno, B., Bhatt, R., Spangenberg, D., and
435   Pallkonda, R.: Analysis and Automated Detection of Ice Crystal Icing Conditions Using Geostationary Satellite Datasets and In Situ Ice Water Content Measurements, SAE Technical Paper 2019-01-1953, doi:10.4271/2019-01-1953, 2019.

Benjamin, S. G., Weygandt, S. S., Brown, J. M., Hu, M., Alexander, C. R., Smirnova, T. G., Olson, J. B., James, E. P., Dowell, D. C., Grell, G. A., Lin, H., Peckham, S. E., Smith, T. L., Moninger, W. R., Kenyon, J. S., and Manakin, G. S.: A North American hourly assimilation and model forecast cycle: The rapid refresh, Mon. Weather. Rev., 144, 1669-1694, doi:
440   10.1175/MWR-D-15-0242.1, 2016.

Bonavita, M., Trémolet, Y., Holm, E., Lang, S. T. K., Chrust, M., Janisková, M., Lopez, P., Laloyaux, P., de Rosnay, P., Fisher, M., Hamrud, M., and English, S.: A Strategy for Data Assimilation. Technical Memo. 800. ECMWF: Reading, UK, 2017.

Brunner, J. C., Ackerman, S. A., Bachmeier, A. S., and Rabin, R. M.: A quantitative analysis of the enhanced-V feature in relation to severe weather, Weather and Forecasting, 22, 853-872, doi: 10.1175/WAF1022.1, 2007.

445   Weygandt, S. S., Alexander, C. R., Dowell, D. C., Hu, M., James, E. P., Benjamin, S. G., Smirnova, T. G., Lin, H., Kenyon, J., and Olson, J. B.: Radar data assimilation impacts in the RAP and HRRR models, 20th Conf. on Integrated Observing and Assimilation Systems for the Atmosphere, Oceans, and Land Surface (IOAS-AOLS), New Orleans, Louisiana, United States, Amer. Meteor. Soc., 10-14 January 2016. Available online at https://ams.confex.com/ams/96Annual/webprogram/Paper289787.html

450   Churchill, D. D. and Houze Jr, R. A.: Development and structure of winter monsoon cloud clusters on 10 December 1978. J. Atmos. Sci., 41, 933-960, doi: 10.1175/1520-0469(1984)041<0933:DASOWM>2.0.CO;2, 1984.

Dworak, R., Bedka, K., Brunner, J., and Feltz, W.: Comparison between GOES-12 overshooting-top detections, WSR-88D radar reflectivity, and severe storm reports, Weather and Forecasting, 27, 684-699, doi: 10.1175/WAF-D-11-00070.1, 2012.

Geer, A., Ahlgrimm, M., Bechtold, P., Bonavita, M., Bormann, N., English, S., Fielding, M., Forbes, R., Hogan, R., Hólm, E.,

455   Janisková, M., Lonitz, K., Lopez, P., Matricardi, M., Sandu, I., and Weston, P.: Assimilating observations sensitive to cloud and precipitation. Technical Memo. 815. ECMWF: Reading, UK, 2017.

GOES-R Series Data Book, 2019. Available from: https://www.goes-r.gov/resources/docs.html

Gustafsson, N., Janjić, T., Schraff, C., Leuenberger, D., Weissman, M., Reich, H., Brousseau, P., Montmerle, T., Wattrelot, E., Bučánek, A., Mile, M., Hamdi, R., Lindskog, M., Barkmeijer, J., Dahlbom, M., Macpherson, B., Ballard, S., Inverarity,

460   G., Carley, J., Alexander, C., Dowell, D., Liu, S., Ikuta, Y. and Fujita, T.: Survey of data assimilation methods for convective-scale numerical weather prediction at operational centres. Q. J. R. Meteorol. Soc. 144, 1218-1256, doi:10.1002/qj.3179, 2018.

Jones, T. A., Knopfmeier, K., Wheatley, D., Creager, G., Minnis, P., and Palikonda, R.: Storm-scale data assimilation and ensemble forecasting with the NSSL experimental warn-on-forecast system. Part II: Combined radar and satellite data experiments. Weather and Forecasting, 31, 297-327, doi: 10.1175/WAF-D-15-0107.1, 2016.

465   Lee, S., Han, H., Im, J., Jang, E., and Lee, M.-I.: Detection of deterministic and probabilistic convection initiation using Himawari-8 Advanced Himawari Imager data. Atmos. Meas. Tech., 10, 1859–1874, https://doi.org/10.5194/amt-10-1859-2017, 2017.

Mecikalski, J. R. and Bedka, K.: Forecasting convective initiation by monitoring the evolution of moving cumulus in daytime GOES imagery. Mon. Weather Rev., 134, 49–78, doi: 10.1175/MWR3062.1, 2006.

470   Mecikalski, J. R., MacKenzie Jr, W. M., Koeing, M., and Muller, S.: Cloud-top properties of growing cumulus prior to convective initiation as measured by Meteosat Second Generation. Part I: Infrared fields. J. Appl. Meteor. Climatol. 49, 521-534, doi: 10.1175/2009JAMC2344.1, 2010.

Migliorini, S., Lorenc, A. C., and Bell, W.: A moisture-incrementing operator for the assimilation of humidity and cloud-sensitive observations: formulation and preliminary results. Q. J. R. Meteorol. Soc. 144, 443-457, doi:10.1002/qj.3216, 2018.

475   Minnis P. and Heck, P. W.: GOES-R Advanced Baseline Imager (ABI) Algorithm theoretical basis document for nighttime cloud optical depth, cloud particle size, cloud ice water path, and cloud liquid water path, 2012. Available from: https://www.goes-r.gov/products/baseline-cloud-opt-depth.html

Müller, R., Haussler, S., and Jerg, M.: The role of NWP filter for the satellite based detection of cumulonimbus clouds. Remote Sens., 10(3), 386, doi: 10.3390/rs10030386, 2018.

480   Müller, R., Haussler, S., Jerg, M., and Heizenreder, D.: A Novel Approach for the Detection of Developing Thunderstorm Cells. Remote Sens., 11(4), 443, doi: 10.3390/rs11040443, 2019.

Qi, Y., Zhang, J., and Zhang, P.: A real-time automated convective and stratiform precipitation segregation algorithm in native radar coordinates. Q.J.R. Meteorol. Soc., 139, 2233-2240, doi: 10.1002/qj.2095, 2013.

Scheck, L., Weissmann, M., and Bach, L.: Assimilating visible satellite images for convective-scale numerical weather

485   prediction: A case-study. Q.J.R. Meteorol. Soc. Advance online publication. doi:10.1002/qj.3840, 2020.

Setvák, M., Rabin, R. M., and Wang, P. K.: A real-time automated convective and stratiform precipitation segregation algorithm in native radar coordinates. Q.J.R. Meteorol. Soc., 139, 2233-2240, doi: 10.1002/qj.2095, 2007.

Sieglaff, J. M., Cronce, L. M., Feltz, W. F., Bedka, K., Pavolonis, M. J., and Heidinger, A. K.: Nowcasting convective storm initiation using satellite-based box-averaged cloud-top cooling and cloud-type trends. J. Appl. Meteor. Climatol., 50, 110-126,

490   doi: 10.1175/2010JAMC2496.1, 2011.

Smith, T. J., Griffith, P., Gunshor, M. M., Daniels, J. M., Goodman, S. J., and Lebair, W. J.: A closer look at the ABI on the GOES-R Series. Bull. Amer. Meteor. Soc., 98, 681-698, doi: 10.1175/BAMS-D-15-00230.1, 2017.

Steiner, M., Houze Jr, R. A., and Yuter, S. E.: Climatological characterization of three-dimensional storm structure from operational radar and rain gauge data. J. Appl. Meteor., 34, 1978-2007, doi: 10.1175/1520-

495   0450(1995)034<1978:CCOTDS>2.0.CO;2, 1995.

Tao, W-K, Simpson J., Lang, S., McCumber, M., Adler, R., and Penc, R.: An algorithm to estimate the heating budget from vertical hydrometeor profiles. J. Appl. Meteor, 29, 1232-1244, doi: 10.1175/1520-0450(1990)029<1232:AATETH>2.0.CO;2, 1990.

Petković, V., Orescanin, M., Kirstetter, P., Kummerow, C., Ferraro, R.: Enhancing PMW satellite precipitation estimation:

500   detecting convective class. J. Atmos. Oceanic Technol., 36, 2349-2363, doi: 10.1175/JTECH-D-19-0008.1, 2019.

Yano, J-I, Ziemiański, M. Z., Cullen, M., Termonia, P., Onvlee, J., Bengtsson, L., Carrassi, A., Davy, R., Deluca, A., Gray, S. L., Homar, V., Köhler, M., Krichak, S., Michaelides, S., Phillips, V. T. J., Soares, P. M. M., and Wzszogrodzki, A. A.: Scientific challenges of convective-scale numerical weather prediction. Bull. Amer. Meteor. Soc., 99, 699-710, doi: 10.1175/BAMS-D-17-0125.1, 2018.

505   Zhang, J., Langston, C., and Howard, K.: Brightband identification based on vertical profiles of reflectivity from the WSR-88D. J. Atmos. Ocean. Technol., 25, 1859-1872, doi: 10.1175/2008JTECHA1039.1, 2008.

Zhang, J. and Qi, Y.: A real-time algorithm for the correction of brightband effects in radar-derived QPE. J. Hydrometeor., 11, 1157-1171, doi: 10.1175/2010JHM1201.1, 2010.

Zhang, J., Howard, K., Langston, C., Kaney, B., Qi, Y., Tang, L., Grams, H., Wang, Y., Cocks, S., Martinaitis, S., Arthur, A.,

510   Cooper, K., Brogden, J., and Kitzmiller, D.: Multi-Radar Multi-Sensor (MRMS) quantitative precipitation estimation: Initial operating capabilities. Bull. Amer. Meteor. Soc., 97, 621-638, doi: 10.1175/BAMS-D-14-00174.1, 2016.

Zinner, T., Mannstein, H., and Tafferner, A.: Cb-TRAM: Tracking and monitoring severe convection from onset over rapid development to mature phase using multi-channel Meteosat-8 SEVIRI data, Meteorol. Atmos. Phys., 101, 191–210, doi:10.5194/amt-6-1903-2013, 2008.

515   Zinner, T., Forster, C., de Coning, E., and Betz, H.-D.: Validation of the Meteosat storm detection and nowcasting system Cb-TRAM with lightning network data – Europe and South Africa, Atmos. Meas. Tech., 6, 1567–1583, doi:10.5194/amt-6-1567-2013, 2013.

520

525
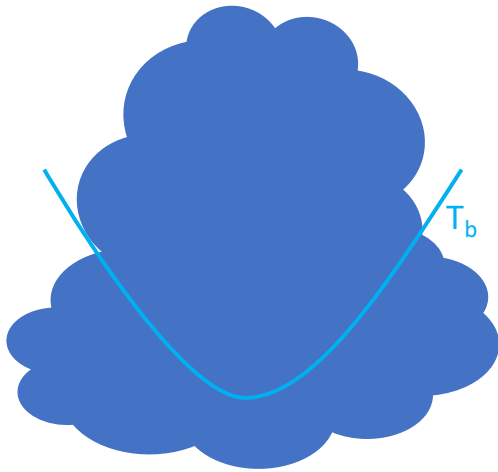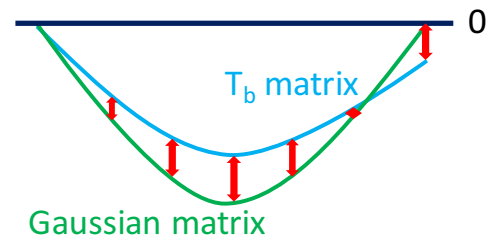
530   **Figure 1: (a) A typical shape of a convective cloud and its T_b distribution around the convective core (blue line). (b) Schematic representation of distributions of the inverted Gaussian matrix (green) and the T_b matrix (blue) when the cloud is convective.**

535
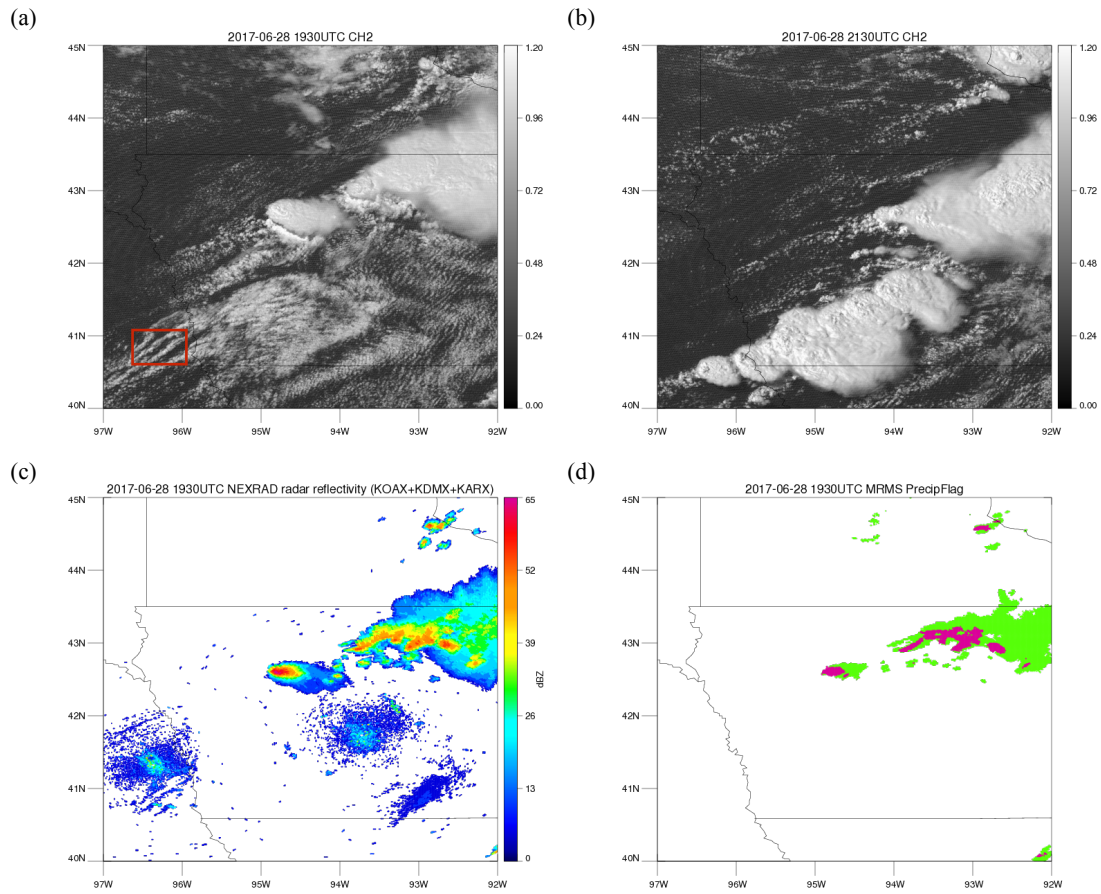
Figure 2: (a) GOES-ABI 0.65µm visible channel imagery (0.5km) at 1930UTC 28 June 2017 over Iowa. Numbers on the colorbar represent reflectances. The red box indicates regions where two convective cells are detected by the GOES T_b method. (b) GOES-ABI 0.65µm visible channel imagery at 2130UTC 28 June 2017. (c) NEXRAD composite reflectivity (KOAX, KDMX, and KARX) around 1930UTC 28 June 2017. (d) MRMS PrecipFlag at 1930UTC 28 June 2017. Pink represents convective while green represents stratiform.

545

550
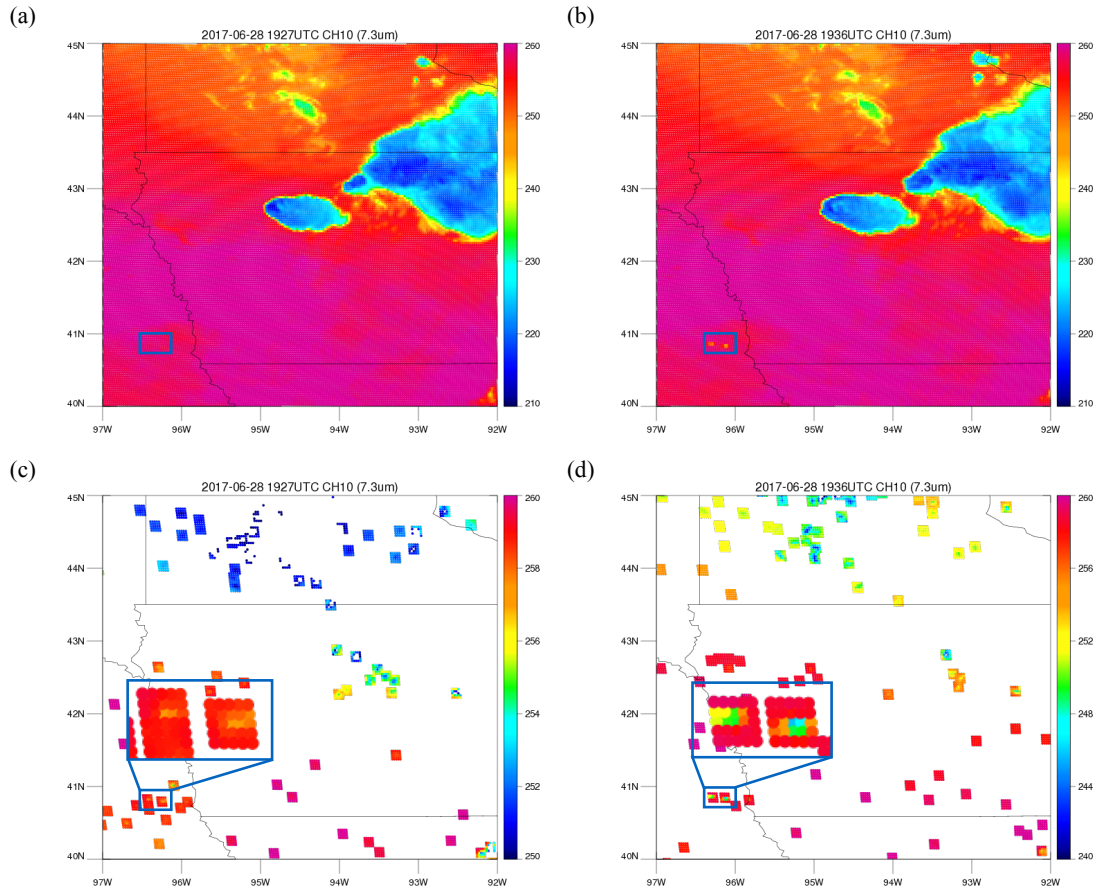
Figure 3: (a) GOES-ABI 7.3μm infrared channel imagery (K) at 1927UTC 28 June 2017. White circle denotes regions where two convective clouds start to grow. (b) Same as figure 3a, but at 1936UTC. (c) T_b matrices obtained from channel 10 (7.3μm) that have the Gaussian shape at 1927UTC 28 June 2017. Blue circle denotes the same region as the white circle in figure 3a.
555 **Note that the scale of the colorbar is adjusted from figure 3a and 3b to better observe convective initiation. (d) Same as figure 3c, but at 1936UTC.**

560
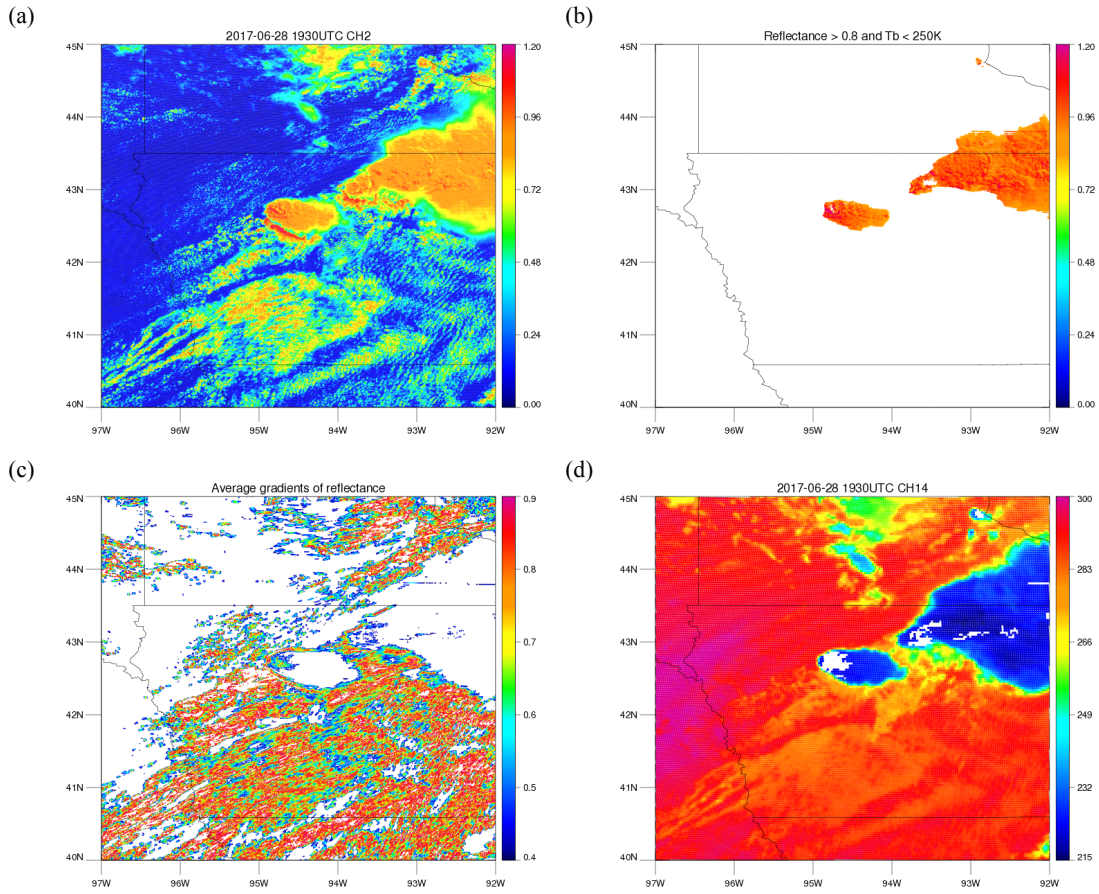
Figure 4: (a) Same as Figure 2a, but using different color table. (b) From the reflectance map in figure 4a, regions that have reflectances over 10 minutes less than 0.8 or have T_bs greater than 250K over 10 minutes are assigned reflectance of zero, and therefore colored in white. (c) Map of average gradients of reflectances over 10 minutes. Regions with average gradient less than 0.4 or greater than 0.9 are colored in white. (d) GOES-ABI 11.2μm infrared channel imagery (K) at 1930UTC 28 June 2017. Regions that passed two criteria from figure 4b and 4c are colored in white.

590

595

600

605
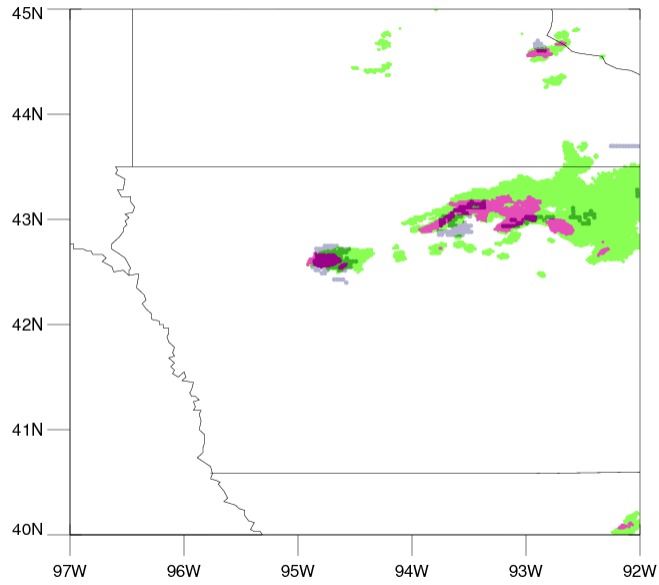
Figure 5: Convective regions detected by GOES-16 (white regions in Fig. 4d) are colored in navy on top of MRMS PrecipFlag at 2230UTC 18 June 2018 (Same figure on Fig. 2d. Pink represents convective while green represents stratiform)

610

615

620
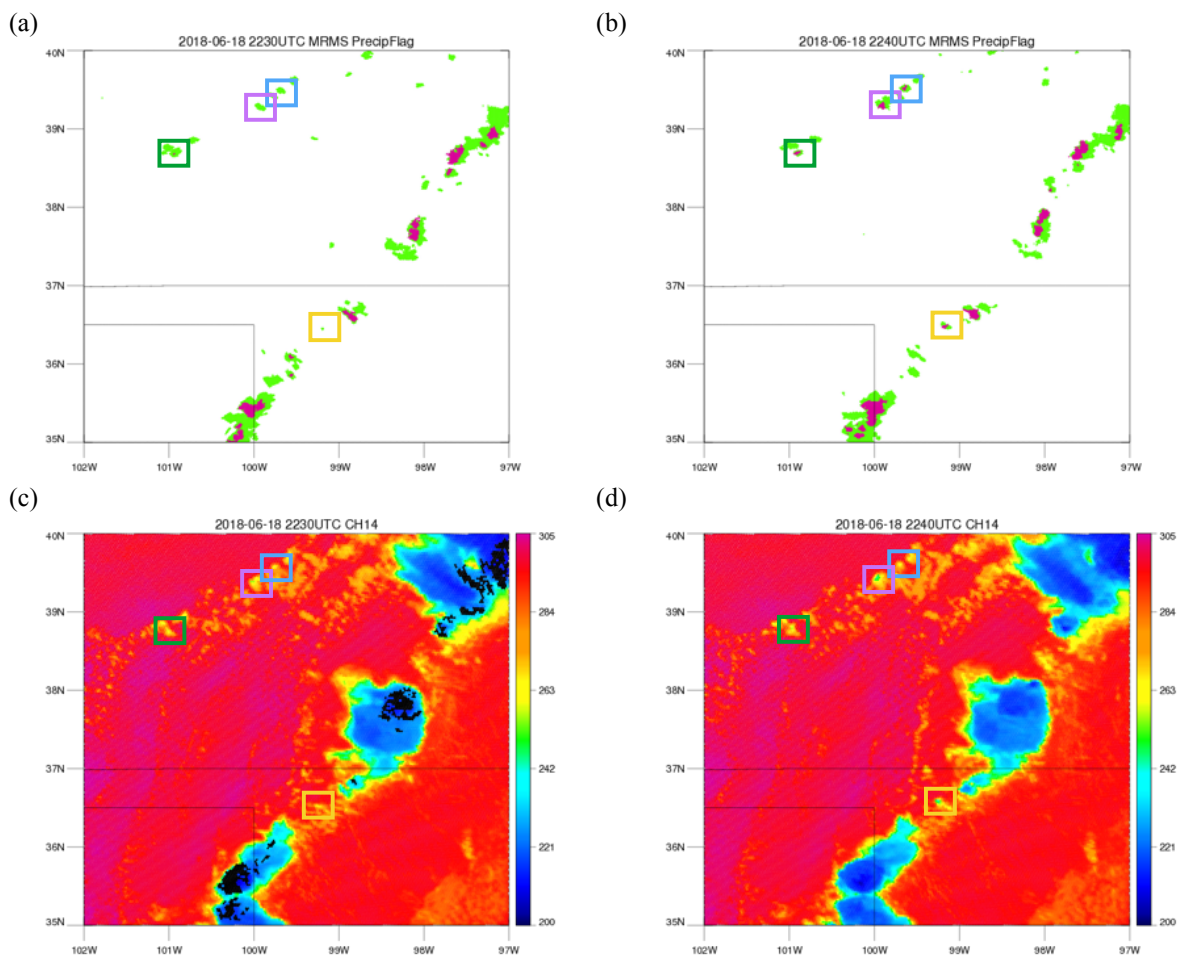
Figure 6: (a) MRMS PrecipFlag at 2230UTC 18 June 2018. Pink represents convective while green represents stratiform. (b) Same as figure 5a, but at 2240UTC. (c) GOES-ABI 11.2μm infrared channel imagery (K) at 2230UTC 18 June 2018 over the Great Plains. (d) Same as figure 5c, but at 2240UTC.

640

645
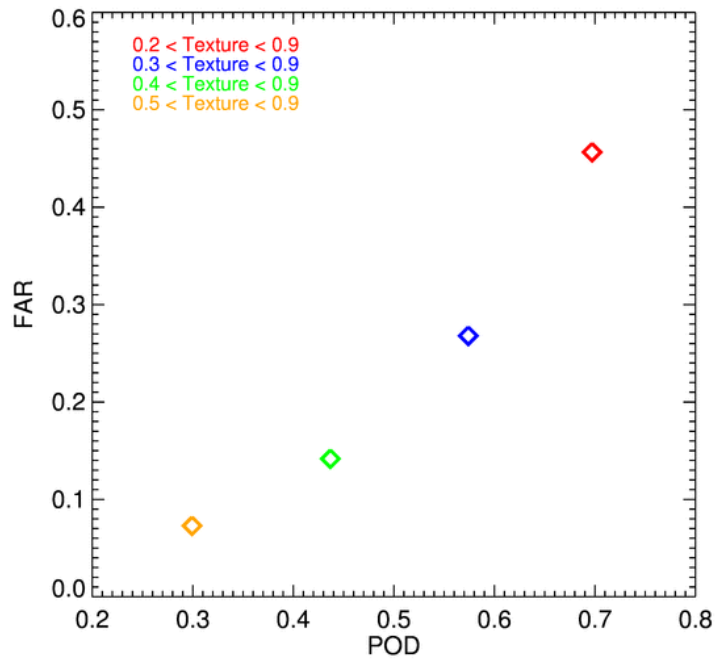
Figure 7: (a) Plot of probability of detection (POD) and false alarm ratio (FAR) using different texture thresholds.

650

655

(a)

(b)
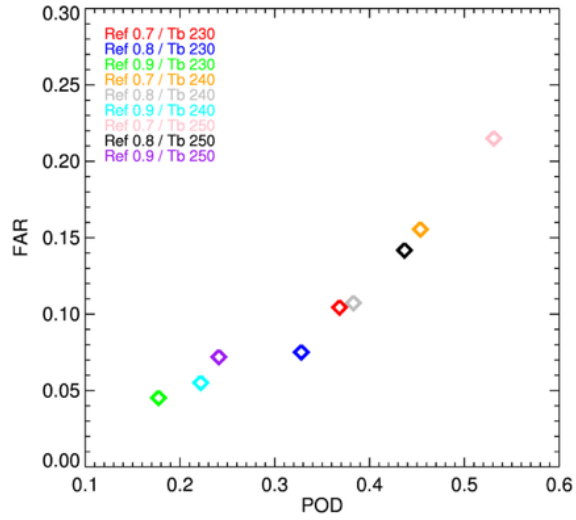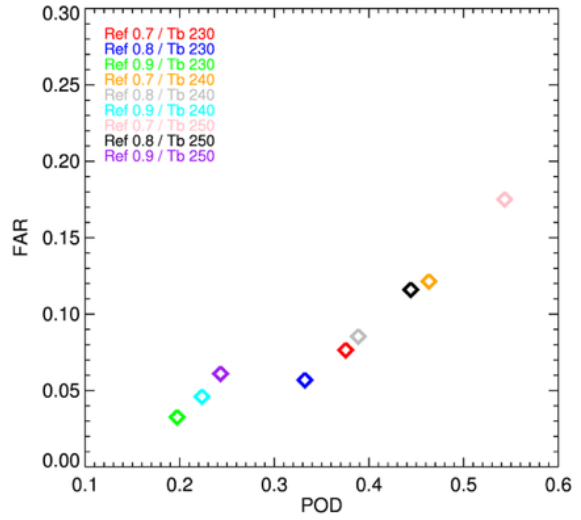
Figure 8: (a) Plot of probability of detection (POD) and false alarm ratio (FAR) for different combinations of T_b and reflectance thresholds. (b) Same as figure 7a, but including MRMS dataset 10 minutes after the detection period.

660

665

670
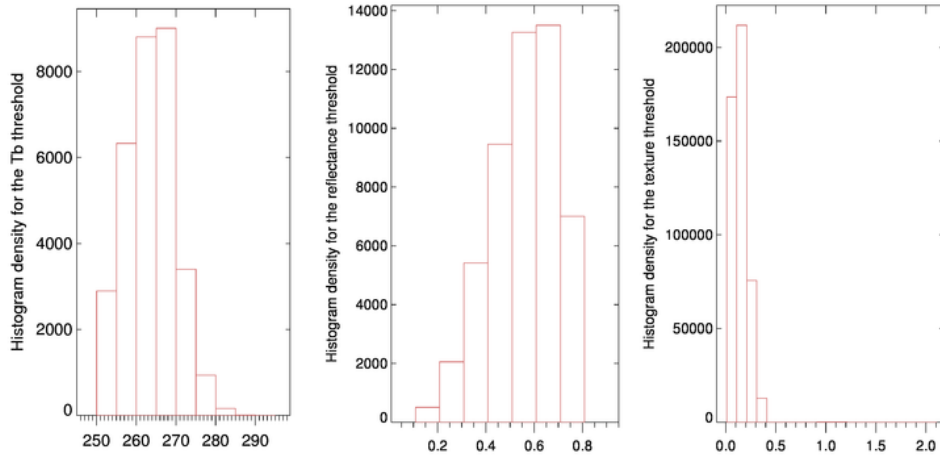
Figure 9: Histograms of T$_b$, reflectance, and texture values when the pixel was not detected by the GOES detecting method due to each of the thresholds.

675

680

685

690

Table 1. Contingency table of results applying both methods to one-month data. C and NC represent convective and non-convective, respectively.

	MRMS-C	MRMS-NC
GOES-C	2.73%	0.46%
GOES-NC	3.30%	93.51%

Table 2. Number of non-convective, convective, convective within 10 minutes, and convective within 20 minutes for using different threshold values (channel 8)

Threshold value (K/min)	Non-convective	Convective	Convective within 10 min	Convective within 20 min (overall accuracy)
-0.1	2635	1465	1610	1678 (38.9%)
-0.2	632	1099	1182	1212 (65.7%)
-0.3	269	848	913	933 (77.6%)
-0.4	137	664	706	715 (83.9%)
-0.5	83	531	561	568 (87.3%)
-0.6	47	443	468	473 (91.0%)
-0.7	27	354	375	378 (93.3%)
-0.8	15	290	305	308 (95.4%)
-0.9	11	233	246	249 (95.8%)
-1.0	7	190	202	204 (96.7%)
-1.1	7	162	171	173 (96.1%)
-1.2	3	133	139	141 (97.9%)
-1.3	1	105	108	109 (99.9%)
-1.4	0	80	83	84 (100.0%)
-1.5	0	64	66	67 (100.0%)
-1.6	0	53	55	55 (100.0%)
-1.7	0	44	46	46 (100.0%)
-1.8	0	35	36	36 (100.0%)
-1.9	0	28	28	28 (100.0%)
-2.0	0	21	21	21 (100.0%)

Table 3. Number of non-convective, convective, convective within 10 minutes, and convective within 20 minutes for using different threshold values (channel 10)

Threshold value (K/min)	Non-convective	Convective	Convective within 10 min	Convective within 20 min (overall accuracy)
-0.1	15444	2727	3228	3461 (18.3%)
-0.2	6110	2085	2377	2499 (29.0%)
-0.3	2862	1677	1869	1944 (40.4%)
-0.4	1443	1354	1477	1526 (51.4%)
-0.5	836	1126	1208	1241 (59.7%)
-0.6	520	947	1008	1031 (66.5%)
-0.7	305	794	839	856 (73.7%)
-0.8	211	666	701	713 (77.2%)
-0.9	135	562	587	597 (81.6%)
-1.0	86	475	497	504 (85.4%)
-1.1	57	406	426	433 (88.4%)
-1.2	40	339	354	359 (90.0%)
-1.3	27	276	289	293 (91.6%)
-1.4	20	244	256	259 (92.8%)
-1.5	13	196	207	209 (94.1%)
-1.6	6	179	189	191 (97.0%)
-1.7	5	151	160	161 (97.0%)
-1.8	4	131	136	137 (97.2%)
-1.9	3	108	112	112 (97.4%)
-2.0	2	90	94	94 (97.9%)

710

715

720

725

730

735